Research Square

Preprints are preliminary reports that have not undergone peer review.
They should not be considered conclusive, used to inform clinical practice,
or referenced by the media as validated information.

Plasma screening of atomic energy levels to ten billion atmospheres

Gilbert Collins

gcollins@lle.rochester.edu

University of Rochester

David Bishel

Livermore National Lab

Philip Nilson

University of Rochester https://orcid.org/0000-0002-9016-8055

David Chin

University of Rochester https://orcid.org/0000-0003-0118-7690

E. Smith

University of Rochester

J. Ruby

University of Rochester

Ed Marley

LLNL

M. Signor

University of Rochester

Reuben Epstein

Laboratory for Laser Energetics

S. Hu

University of Rochester https://orcid.org/0000-0003-2465-3818

M. Gu

Prism Computational Sciences

I. Golovkin

Prism Computational Sciences https://orcid.org/0000-0002-4985-0386

Ryan Rygg

University of Rochester https://orcid.org/0000-0002-0605-7847

Article

Keywords:

Posted Date: August 22nd, 2026

DOI: https://doi.org/10.21203/rs.3.rs-6323542/v1

License: This work is licensed under a Creative Commons Attribution 4.0 International License.
Read Full License

Additional Declarations: There is **NO** Competing Interest.

Plasma screening of atomic energy levels to ten billion atmospheres

D. T. Bishel,[1,2,3,*] P. M. Nilson,[2] D. A. Chin,[1,2] E. A. Smith,[1,2] J. J. Ruby,[4] E. V. Marley,[3] M. Signor,[1,2] R. Epstein,[2] S. X. Hu,[1,2,4] M. F. Gu,[5] I. E. Golovkin,[5] J. R. Rygg,[1,2,4] and G. W. Collins[1,2,4]

[1]*Department of Physics and Astronomy, University of Rochester, Rochester, New York 14627, USA*
[2]*Laboratory for Laser Energetics, University of Rochester, Rochester, New York 14623, USA*
[3]*Lawrence Livermore National Laboratory, Livermore, California 94550, USA*
[4]*Department of Mechanical Engineering, University of Rochester, Rochester, New York 14627, USA*
[5]*Prism Computational Sciences, 455 Science Drive, Madison, WI, 53711, USA*

At atmospheric pressures the atom is typically considered immutable with known energy levels for electrons; however, in the deep interiors of stars where atoms exist at and beyond the atomic unit of pressure, i.e. hundreds of millions to billions of atmospheres pressure,[1] the atom is fundamentally changed. At such conditions, unbound electrons are squeezed interior to core orbitals of the atom, screening the nuclear charge and dramatically shifting the quantum energy levels for electrons.[2–5] The plasma becomes integral to the structure and properties of the atom, a regime that is challenging for today's theoretical tools and where benchmark data are needed.[6,7] We present the first such data, mapping the electron configuration of the inner most orbitals of highly–ionized chromium to pressures of 10 billion atmospheres (1 petapascal) and temperatures of 400 eV (4×10^6 K). Time-resolved x-ray absorption measurements reveal a 20-eV shift in core electron bound-bound transitions, due to electron screening from the plasma. This shift together with a simple atomic physics model provides the first constraints for electron screening on atomic orbitals at and beyond atomic pressures. This shift is consistent with a charge of $0.17e$ ($0.005e$) penetrating the $2p$ ($1s$) orbit of Cr. These results also reveal a shortcoming in *ab-initio* density functional theory modeling of atomic structure and radiative transitions at these extreme conditions.

At sufficiently high pressures and densities, unbound electron correlations are integral to the nature of bound atomic orbitals. Understanding this plasma-atom interplay is central to accurate equations of state (EOS) and transport models for stars and inertial fusion implosions, yet out of reach for first principles theory. While conventional wavefunction calculations consider screening of the nuclear charge by the bound electrons,[8] unbound plasma electrons that are compressed interior to the bound orbits produce additional screening and reduce binding energies.[3] The reduction of the binding energy is known as ionization potential depression (IPD) or continuum lowering (CL), which manifests in a shift of the photoionization edge to lower photon energies[9–11] and in enhanced ionization.[12–16] A dense plasma environment can also differentially perturb the bound electronic state eigenvalues, resulting in a spectral line shift known as the plasma polarization shift (PPS).[2] Modeling the integral effect of screening (IPD, CL, and PPS) as well as Stark effects should include spatial, temporal, and fluctuating distributions, which together are beyond today's *ab initio* capabilities for the multitude of atomic states involved. Experimental line shift data exist for electron densities $\lesssim 10^{24}$ cm^{-3},[17–21], while recent CL measurements have seemingly inconsistent results.[9,10,16] Thus, benchmark data for plasma screening at atomic pressures, its effect on atomic wavefunctions, and the resulting perturbation of radiative transition energies, are essential for guiding the theory of dense plasmas and understanding the deep interiors of stars[22,23] and the late stages of inertial confinement fusion implosions[24] (Fig. 1).

To address this experimental gap and benchmark the response of atomic wavefunctions to petapascal pressures, spherical implosions of capsules hosting a buried chromium ($_{24}$Cr) layer were performed at the OMEGA-60 facility.[30] A laser pulse of 25.9 kJ delivered in 1 nanosecond uniformly illuminated the 30-μm–thick, 440-μm–outer-radius CH shell containing 0.1-μm–thick Ni and Cr layers recessed 8 μm from the inner surface (Fig. 2 (a)). The hollow shell was filled with 2 atm of deuterium (D_2) gas at room temperature and doped with 1% (per atom) of Kr.

The dynamics of the implosion are illustrated by the 1-D radiation-hydrodynamic simulations in Fig. 2. The shell is initially compressed then accelerated by the 1-ns laser pulse (Fig. 2(e), solid grey) to a maximum velocity of 230 km/s. The imploding shell then compresses and heats the gaseous core to pressures exceeding 100 TPa and temperatures exceeding 1 keV (Fig. 2 (b,f)) (2.0 ns). This hot core produces a bright, multi-keV x-ray source that penetrates and escapes the surrounding dense shell with peak x-ray production coincident with the peak core temperature (Fig. 2 (f,h)). The 100-TPa pressure within the hot spot exceeds that of the shell and launches a compression wave moving outward that steepens into a shock ("shock formation," Fig. 2 (b)), compressing and heating the Cr layer ("shock impact," Fig. 2 (c), (g)).

X-rays emitted by the hot, stagnated core that transport out through the cold, dense shell were recorded by a

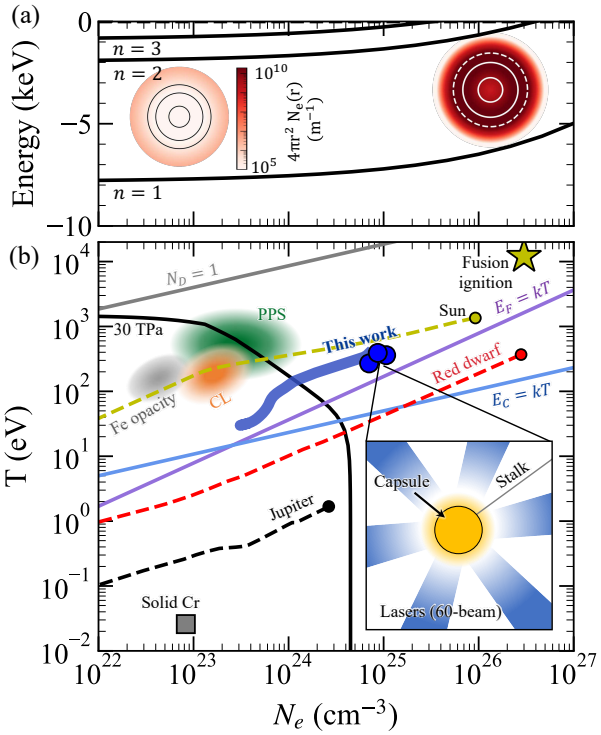


FIG. 1. **Energy level perturbations in the atomic pressure regime.** (a) Density dependence of the $n = 1$ through 3 energy levels of H-like Cr embedded in a uniform electron gas. The insets show the radial electron distribution $4\pi r^2 N_e(r)$ for spatially averaged $N_e = 10^{20}$ cm^{-3} and 10^{26} cm^{-3} with respect to the mean orbital radii of $n = 1$ through 3 bound states (solid lines). Binding energies are reduced as, with increasing density, more free electrons penetrate core orbitals and screen the nuclear charge. By $N_e = 10^{26}$ cm^{-3}, the $n = 3$ state becomes unbound (dashed line). (b) Temperature–electron-density phase diagram with the solid contours of the atomic pressure isobar (30 TPa) for Cr (black), Coulomb energy $E_C = \frac{e^2}{4\pi\epsilon_0}(4\pi N_e/3)^{1/3} = kT$ (light blue), Fermi energy $E_F = \frac{\hbar^2}{2m_e}(3\pi^2 N_e)^{2/3} = kT$ and Debye number $N_D = N_i \frac{4\pi}{3}(\frac{\epsilon_0}{kT}\frac{1}{(Z^*)^2 N_i e^2})^{3/2} = 1$ with a representative ion charge of $Z^* = N_e/N_i = 18$ (grey); the dashed thermodynamic profiles of the Sun[25] (yellow), the red dwarf Proxima Centauri[26] (red), and Jupiter[27] (black); conditions of ambient Cr (grey square); and the states of an ignited NIF capsule[24] (yellow star). Simulated (blue band) and inferred (blue circles) conditions of OMEGA implosions of this work. Prior atomic spectroscopic measurements near $N_e = 10^{23} - 10^{24}$ cm^{-3} (shaded)[9,18,28,29] have revealed discrepancies with state-of-the-art atomic models. The results of this letter help bridge the gap between previous electron screening measurements [PPS[18,29] (green) and CL[9] (orange)] and solar-core conditions.

flat-crystal spectrometer coupled to an x-ray streak camera configured to measure the Cr K-shell spectral band ($h\nu \approx 5$ keV). This core flash ($1.7 - 2.3$ ns) encodes the evolution of the Cr layer as the return shock propagates outward (Fig. 2 (i)). Before the Cr is impacted and heated by the return shock, the Cr ions are weakly to moderately ionized (neutral to Ne-like Cr^{14+}) with fully occupied $2p$ orbitals. Vacancies in the Cr $1s$ orbital are produced by high-energy x-rays emitted by the D_2-Kr hot-spot, enabling subsequent $2p - 1s$ fluorescence transitions ($1.8-2.1$ ns). These transitions of neutral through Ne-like Cr^{14+} all lie in the photon energy range between 5410 and 5440 eV. Transitions from neighboring ionization states are not spectrally resolved.

Once the return shock impacts the Cr (2.1 ns), the temperature is sufficient to produce vacancies in the $2p$ orbital, including the ground state and multiply-excited states of open L-shell ions (F-like Cr^{15+} to Li-like Cr^{21+}). The $2p$ vacancies enable the distinct $1s - 2p$ absorption features visible from 2.0 ns through the end of the core flash. Each $1s - 2p$ absorption feature is composed of unresolved transitions from a particular $n = 1$ and $n = 2$ configuration together with lower ionization states with electrons populating $n > 2$ shells. Each blended feature is labeled according to the $n = 1$ and $n = 2$ configuration. For example, all $1s-2p$ absorption transitions from two electrons in the $n = 1$ and one electron in the $n = 2$ shell, i.e. $1s^2\ 2s$, together with any allowed electron populations in shells $n > 2$, contribute to what we call the "Li-like" absorption feature. Since each absorption feature is resolved from its neighbors, they can be labeled from F-like Cr^{15+}, being the least ionized ground-state configuration with a $2p$ vacancy and having the lowest energy transition, through Li-like Cr^{21+}.

The line absorption of Cr reveals significant energy shifts relative to zero-density ("isolated atom") values[32] (Fig. 3 (a)) due to screening in the dense plasmas. By solving the radiative transfer equation, a model of the spectrum is parametrized in terms of the implosion geometry, thermodynamic conditions, and opacity. Forward modeling the measured spectra constrains the spectral line shifts relative to zero-density values, the much smaller Doppler shift due to shell motion, and the apparent shift due to multiply excited satellites. A peak temperature $T_e = 391 \pm 18$ eV and spatially-averaged free electron density $N_e = (1.06 \pm 0.29) \times 10^{25}$ cm^{-3} are inferred, where uncertainties correspond to the 68% highest-density interval (HDI) of the respective posterior distributions (see Supplemental Matierals). Inferred velocities of the Cr are less than 150 km/s. The spectral model thus constrains the sum of the Doppler and satellite shift components to be less than a few eV ($< 10\%$ of the observed shift), shown for the B-like ionization state in Fig. 3 (b). The residual shift due to screening is of order 20 eV for all ionization states (see Supplemental Materials).

The degree to and manner in which transition energies (and thus the wavefunctions) are perturbed depends critically on how the free electrons are distributed in space. Any model of the dense plasma environment must

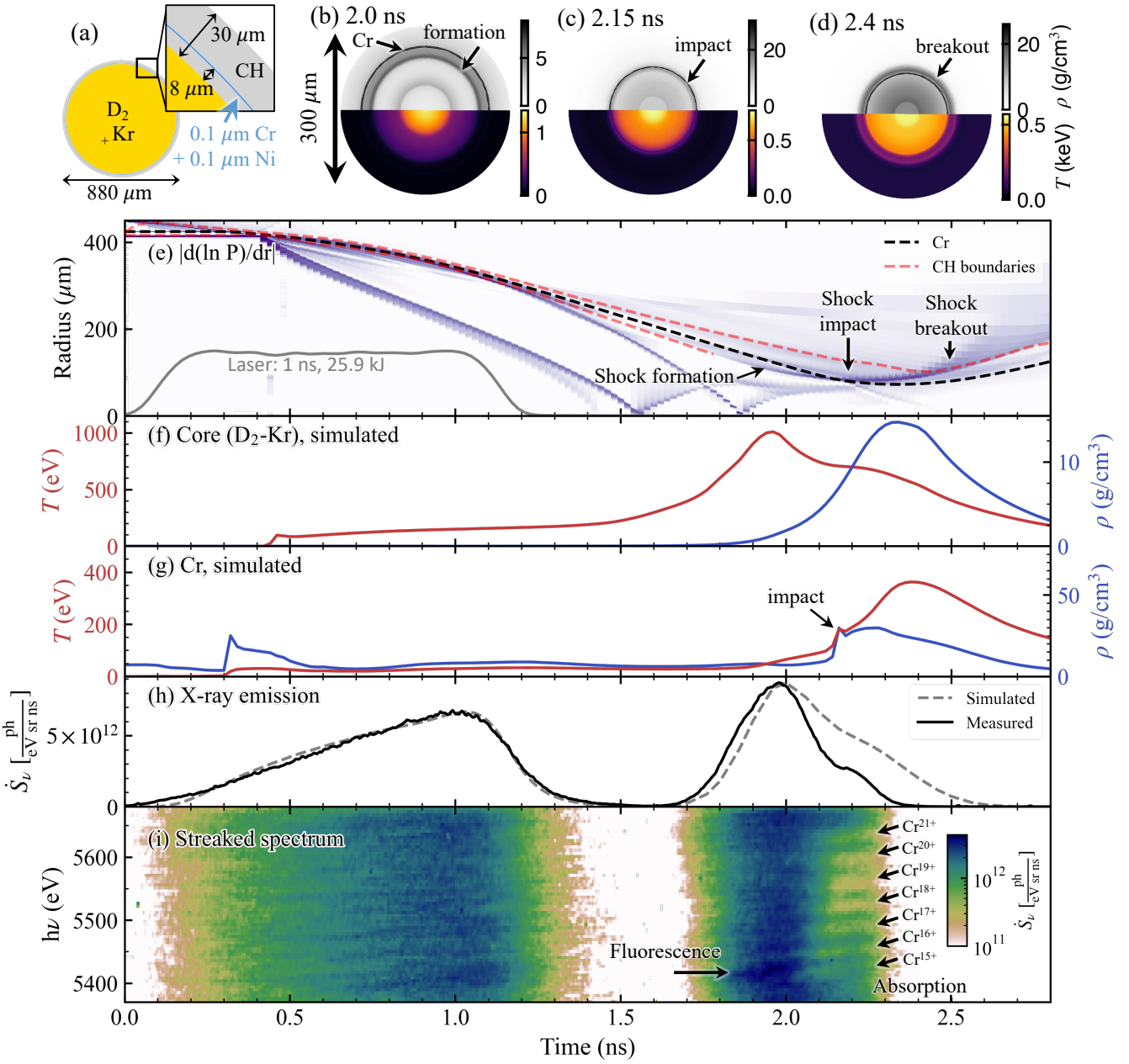


FIG. 2. **Experimental overview and streaked spectra.** (a) Initial fabricated capsule. Density (top, g/cm^3) and temperature (bottom, keV) of the capsule from a hydrodynamic simulation (b) as the return shock forms, (c) as the shock impacts the Cr, and (d) as the shock breaks out. (e) Trajectory of the dense plastic shell (dashed red) and Cr and Ni layers (dashed black), with laser pulse (solid grey). The false colormap of $|\frac{\mathrm{d}\ln P}{\mathrm{d}r}|$ visualizes the return shock from formation through impact until eventual breakout. Average temperature T (red) and density ρ (blue) of (f) the core and (g) the Cr layer; impact of the Cr by the return shock produces a discontinuous increase in T and ρ. (h) Simulated (dashed grey) and measured (solid black) x-ray source emission near 5 keV. The simulated x-ray source emission was calculated by solving the equation of radiative transfer along parallel rays through a spherically symmetric, 3D representation of the 1D LILAC simulations at each time and integrating the result over area. The D2/Kr core and CH layers used tabulated non–local-thermodynamic-equilibrium (non-LTE) opacities, while PrismSPECT[31] was used to construct an opacity table of Cr that includes $1s-2p$ transitions. (i) Streaked spectrum with Cr $2p-1s$ fluorescence ($h\nu \approx 5420$ eV) observable prior to 2.1 ns and $1s-2p$ absorption at higher photon energies after 2.1 ns. Onset of absorption coincides with shock compression of the Cr layer.

make an *ansatz* regarding this plasma distribution. The electron density distribution derived from first principles

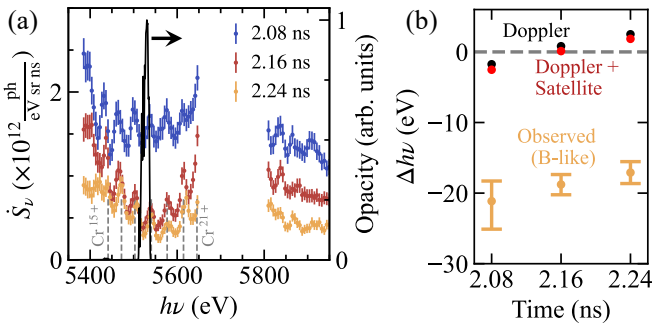


FIG. 3. **Measured absorption spectra and extracted line shifts.** (a) Source emission at different times given by the legend. Error bars denote the standard deviation of the expected signal assuming Poisson noise amplified by the streak camera gain. Dashed grey lines denote the line centroids of the F-like (Cr^{15+}) through Li-like (Cr^{21+}) ionization states calculated from zero-density isolated atom calculations and indicate a red-shift of absorption lines. The gap in the data at 5800 eV is due to a defect on the photocathode. The DFT-based opacity (black) at representative conditions 50 g/cm^3 and 400 eV approximates the observed centroid of the C-like ionization state but fails to capture the breadth of the charge state distribution. (b) Observed shift relative to ground-state isolated-atom FAC calculations for the B-like state (orange) with Doppler and satellite components constrained by the inference. Error bars indicate the quadrature sum of the 68% HDI of the total inferred shift, the Doppler shift, and the satellite shift.

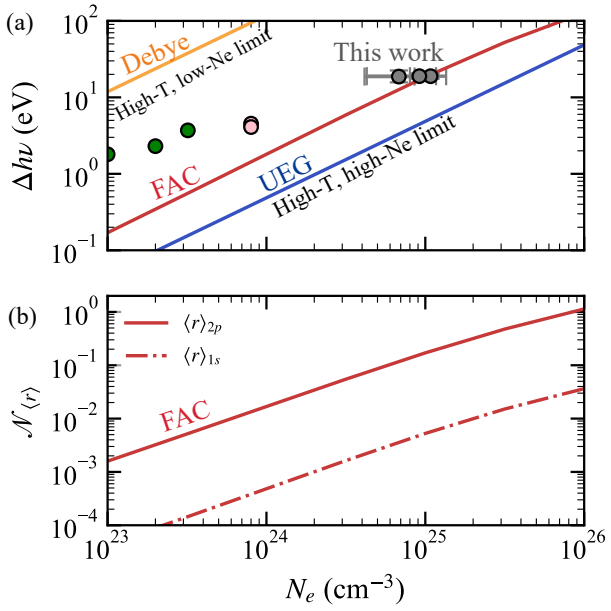


FIG. 4. **Comparison of line shifts to theory.** (a) Line shift for this work in Cr (grey circles) compared to those predicted by Debye (orange), uniform electron gas (blue), and self-consistent potential (red) models for Cr at the observed temperature of 400 eV. Previous work on Al He$_\alpha$ and Ly$_\alpha$ are shown by the green[18] and pink[17] markers. (b) Fraction of the self-consistent free electron wave function penetrating the 1s (dash-dotted) and 2p (solid) orbitals. At the inferred conditions of $N_e = 10^{25}$ cm^{-3} (grey), screening of the nuclear charge by 17% of an electron produces the observed line shift.

within density functional theory (DFT), has been used to explain previous spectroscopic observations in dense plasmas.[14,33] The plasma polarization shift has even been predicted by DFT simulations [see Fig. 8(c) of Karasiev *et al.*[34]] However, our use of a localized Cr layer to mitigate plasma gradients reveals limitations of current DFT methods to provide a complete description of the ionization states of atoms in such dense plasmas. As indicated by the black curve in Fig. 3(a), opacity calculations using band energies from DFT-based molecular-dynamics[14] produce transitions from only the mean ionization state and do not describe the charge state distribution observed in these experiments. We surmise that the DFT calculations converge on the mean ionization state because DFT calculations give only the static, thermally averaged ground-state electron distribution. The ionization and recombination processes which give rise to the ionization state distribution, however, involve dynamic electron excitations which occur on the femtosecond time scale. Ionization state distributions are not accessible from such static DFT calculations. These experimental observations indicate the need for further development of first-principles tools to describe the nature of dense plasmas.

To understand the mechanisms driving the observed line shifts, Fig. 4(a) compares the residual line shifts to those predicted by different plasma models as a function of N_e. The data presented here are intermediate to the predictions in the limiting cases of a high-temperature, high-density uniform electron gas (UEG) and a high-temperature, low-density Debye-screened plasma. This is consistent with the inferred conditions (c.f. Fig. 1), which violate the validity conditions of both models. With less than 0.001 ions lying within a Debye screening length $\lambda_D = \left[\frac{\epsilon_0}{e^2}\frac{k_B T_i}{(Z^*)^2 N_i}\right]^{1/2}$, the Debye model overpredicts the magnitude of screening and thus the magnitude of the line shift. Moreover, the plasma is only near-degenerate ($kT \approx 2E_F$), having insufficient degeneracy pressure for free electrons to distribute uniformly; thus the UEG model underpredicts the magnitude of the line shift.

We see that the residual shift is consistent with the PPS predicted by the the Flexible Atomic Code (FAC),[32] in which the free electron distribution is solved self-consistently with the bound-electron structure,[35] and the ionization is consistent with the IPD of the Ecker-Kröll model.[12] Consistency with the FAC calculation allows a more quantitative inference of how free electrons are distributed about the nucleus and interior to the 1s and 2p orbitals. Fig. 4 (b) shows the fractional charge

$\mathcal{N}_{\langle r\rangle} = \int_0^{\langle r\rangle} \mathrm{d}r\ 4\pi r^2 N_e(r)$ interior to the average $1s$ and $2p$ orbital radii. At the experimental conditions of $T = 400$ eV and $N_e = 10^{25}$ cm^{-3}, a charge of 0.17 e is compressed interior to the $2p$ orbital. Measurement of the line shift at known density constrains the time-averaged, spatial distribution of the free electrons about the nucleus.

These data provide the first constraints of screening in billion-atmosphere (100 TPa) plasmas with many co-existing ionization states. Furthermore, the thermodynamic conditions are inferred through experimental measurements. The simple models shown here provide a description of how the atomic wavefunctions evolve with increasing density and pressure. The isolated line shifts complement measurements of ionization and line broadening to inform screening in dense plasmas. Together these measurements help constrain a holistic screening model at stellar core and inertial confinement fusion conditions.

Spherical implosions are uniquely capable of reaching stellar-core conditions.[36,37] We have leveraged the extreme densities achieved in an implosion shell to interrogate the influence of screening on atomic wavefunctions, providing an avenue to benchmark atomic structure at and beyond the atomic unit of pressure. Data of this type are required to challenge and improve traditional equation of state and opacity models in the dense plasma regime, and in turn the stellar structure and implosion radiation-hydrodynamic codes that rely on them. With the progress in achieving thermonuclear fusion ignition[38,39] and the goal to better understand and harness such fusion implosions, it is important to understand the energy balance, which is mediated in part by the radiation transport through matter at billions of atmospheres (100 TPa). Deployment of these measurements on larger, higher compression implosions accessible at the National Ignition Facility will further extend the densities achievable; even a twofold increase in density would enable study of screening processes in a degenerate plasma, perhaps approaching the uniform-electron-gas limit of the screening models.

* bishel1@llnl.gov

[1] Bukowinski, M. S. T. Quantum Geophysics. *Annual Review of Earth and Planetary Sciences* **22**, 167–205 (1994).

[2] Volonte, S. Polarisation shift effect in high-density plasmas. *Journal of Physics D: Applied Physics* **11**, 1615–1638 (1978).

[3] More, R. M. Electronic Energy Levels in Dense Plasmas. *J. Quant. Spectrosc. Radiat. Transfer* **27**, 345–357 (1982).

[4] Nguyen, H., Koenig, M., Benredjem, D., Caby, M. & Coulaud, G. Atomic structure and polarization line shift in dense and hot plasmas. *Physical Review A* **33**, 1279–1290 (1986).

[5] Li, X. & Rosmej, F. B. Quantum-number-dependent energy level shifts of ions in dense plasmas: A generalized analytical approach. *Europhysics Letters* **99**, 33001 (2012).

[6] Dharma-wardana, M. & Perrot, F. Level shifts, continuum lowering, and the mobility edge in dense plasmas. *Physical Review A* **45**, 5883–5896 (1992).

[7] Murillo, M. S., Weisheit, J., Hansen, S. B. & Dharma-Wardana, M. W. Partial ionization in dense plasmas: Comparisons among average-atom density functional models. *Physical Review E - Statistical, Nonlinear, and Soft Matter Physics* **87**, 1–19 (2013).

[8] Cowan, R. D. *The Theory of Atomic Structure and Spectra* (University of California Press, Berkeley, 1981).

[9] Vinko, S. M. *et al.* Creation and diagnosis of a solid-density plasma with an X-ray free-electron laser. *Nature* **482**, 59–62 (2012).

[10] Ciricosta, O. *et al.* Direct measurements of the ionization potential depression in a dense plasma. *Physical Review Letters* **109**, 065002 (2012).

[11] Crowley, B. J. Continuum lowering - A new perspective. *High Energy Density Physics* **13**, 84–102 (2014).

[12] Ecker, G. & Kröll, W. Lowering of the ionization energy for a plasma in thermodynamic equilibrium. *Physics of Fluids* **6**, 62–69 (1963).

[13] Stewart, J. C. & Pyatt, K. D. Lowering of Ionization Potentials in Plasmas. *Astrophysical Journal* **144**, 1203–1211 (1966).

[14] Hu, S. X. *et al.* Probing atomic physics at ultrahigh pressure using laser-driven implosions. *Nature Communications* **13**, 6780 (2022).

[15] Döppner, T. *et al.* Observing the onset of pressure-driven K-shell delocalization. *Nature* **618**, 270–275 (2023).

[16] Hoarty, D. J. *et al.* Observations of the effect of ionization-potential depression in hot dense plasma. *Physical Review Letters* **110**, 265003 (2013).

[17] Eidmann, K. *et al.* Generation of hot plasma at solid density by high-contrast ultra-short laser pulses. *Journal of Quantitative Spectroscopy and Radiative Transfer* **65**, 173–184 (2000).

[18] Stillman, C. R. *et al.* Picosecond time-resolved measurements of dense plasma line shifts. *Physical Review E* **95**, 1–5 (2017).

[19] Kraus, B. F. *et al.* Solid-Density Ion Temperature from Redshifted and Double-Peaked Stark Line Shapes. *Physical Review Letters* **127**, 205001 (2021).

[20] Hansen, S. B. *et al.* Changes in the electronic structure of highly compressed iron revealed by X-ray fluorescence lines and absorption edges. *High Energy Density Physics* **24**, 39–43 (2017).

[21] Jiang, S. *et al.* Measurements of pressure-induced K_β line shifts in ramp compressed cobalt up to 8 Mbar. *Physical Review E* **101**, 023204 (2020).

[22] Van Horn, H. Dense Astrophysical Plasmas. *Science* **252**, 384–390 (1991).

[23] Kritcher, A. L. *et al.* A measurement of the equation of state of carbon envelopes of white dwarfs. *Nature* **584**, 51–54 (2020).

[24] Zylstra, A. B. *et al.* Experimental achievement and signatures of ignition at the National Ignition Facility. *Physical Review E* **106**, 1–10 (2022).

[25] Bahcall, J. N. & Pinsonneault, M. H. Standard solar models, with and without helium diffusion, and the solar neutrino problem. *Reviews of Modern Physics* **64**, 885–926 (1992).

[26] Lütgert, J. *et al.* Platform for probing radiation transport properties of hydrogen at conditions found in the deep interiors of red dwarfs. *Physics of Plasmas* **29** (2022).
[27] French, M. *et al.* Ab initio simulations for material properties along the Jupiter adiabat. *Astrophysical Journal, Supplement Series* **202** (2012).
[28] Bailey, J. E. *et al.* A higher-than-predicted measurement of iron opacity at solar interior temperatures. *Nature* **517**, 56–59 (2015).
[29] Beiersdorfer, P. *et al.* High-resolution measurements of Cl^{15+} line shifts in hot, solid-density plasmas. *Physical Review A* **100**, 1–5 (2019).
[30] Boehly, T. R. *et al.* Initial performance results of the OMEGA laser system. *Optics Communications* **133**, 495–506 (1997).
[31] MacFarlane, J. J. *et al.* Simulation of the ionization dynamics of aluminum irradiated by intense short-pulse lasers. In Hammel, B. A., Meyerhofer, D. D., Meyer-ter Vehn, J. & Azechi, H. (eds.) *Inertial Fusion Sciences and Applications 2003*, 457–460 (American Nuclear Society, La Grange Park, IL, 2003).
[32] Gu, M. F. The flexible atomic code. *Canadian Journal of Physics* **86**, 675–689 (2008).
[33] Vinko, S. M., Ciricosta, O. & Wark, J. S. Density functional theory calculations of continuum lowering in strongly coupled plasmas. *Nature Communications* **5**, 3533 (2014).
[34] Karasiev, V. V. & Hu, S. X. Unraveling the intrinsic atomic physics behind x-ray absorption line shifts in warm dense silicon plasmas. *Physical Review E* **103**, 1–14 (2021).
[35] Gu, M. F. & Beiersdorfer, P. Stark shift and width of x-ray lines from highly charged ions in dense plasmas. *Physical Review A* **101**, 1–6 (2020).
[36] Ruby, J. J., Gaffney, J. A., Rygg, J. R., Ping, Y. & Collins, G. W. High-energy-density-physics measurements in implosions using Bayesian inference. *Physics of Plasmas* **28**, 032703 (2021).
[37] Bishel, D. T. *et al.* Toward constraint of ionization-potential depression models in a convergent geometry. *High Energy Density Physics* **50** (2024).
[38] Abu-Shawareb, H. *et al.* Lawson Criterion for Ignition Exceeded in an Inertial Fusion Experiment. *Physical Review Letters* **129**, 75001 (2022).
[39] Abu-Shawareb, H. *et al.* Achievement of Target Gain Larger than Unity in an Inertial Fusion Experiment. *Physical Review Letters* **132**, 065102 (2024).

Supplemental Material

Spectrometer Calibration

X-ray emission escaping the capsule was measured by one time-integrated and one time-resolved flat crystal x-ray spectrometer. The time-integrated spectrometer (XRS)[1] used an ammonium dihydrogen phosphate (ADP) Bragg crystal cleaved on the [101] plane with resolving power $E/\Delta E \approx 480$ at 5.4 keV, with image plate (IP) as the recording medium.

The time-resolved spectrometer (SXS)[2] used a pentaerythritol (PET) Bragg crystal cleaved on the [002] plane with a $2d$-spacing of 8.754 $\mathring{A}$ and resolving power $E/\Delta E \approx 230$ at 5.5 keV. SXS was coupled to an x-ray–sensitive streak camera (PJX)[3] with a 5-ns sweep duration and an 80-ps temporal resolution.[4] The time base was measured on a dedicated shot by illuminating a Cr-alloy foil with a comb pulse of optical laser pulses and recording the resulting comb of x-ray pulses. Uncertainty in the time base accumulates as time elapses from an event of known timing; for an elapsed time of 2 ns, the systematic uncertainty is 10 ps.

The streaked dataset was corrected for a 0.15-radian skew in the temporal (horizontal) direction by assuming no spectral dependence in the start and end times of both the coronal emission and the stagnation continuum emission. A skew of 0.01 radians in the spectral (vertical) direction was necessary to ensure that the photocathode defect around 5800 eV remained at constant photon energy throughout the data record. The defect in the photocathode occurs at a fixed spectral location coordinate in the spectrum and encodes aberrations from the streak camera electron optics.

The dispersion and sensitivity of each spectrometer is determined independently from ray traces of the respective spectrometer geometry. The signal of XRS is converted to source emission analogous to the formalism of Marrs *et al*:[5]

$$S_\nu \left[\frac{ph}{sr\ eV}\right] = \frac{D}{k_{IP}\ T_{filt} G(E) A_{pixel}}, \qquad (1)$$

where D is the data (in photostimulated luminescence, or PSL), k_{IP} is the conversion factor from PSL to incident photons,[6] T_{filt} is the filter transmission, and A_{pixel} is the area of a pixel. The spectrometer sensitivity $G(E) = R(E)\frac{dE}{d\theta_B}\frac{d\Omega}{dA}$ is composed of the photon-energy–dependent crystal reflectivity $R(E)$, the derivative of Bragg's law $\mathrm{d}E/\mathrm{d}\theta_B$, and the solid angle of the source projected onto a unit area of the detector $\mathrm{d}\Omega/\mathrm{d}A$.

The signal in PJX is converted to source emission rate similarly:

$$\frac{dS_\nu}{dt}\left[\frac{ph}{s\ sr\ eV}\right] = \frac{D}{k_{pc}\ T_{filt} G(E) A_{eff} t_{dwell}}, \qquad (2)$$

Crystal	PET	ADP
System	Tetragonal	Tetragonal
C_{11}	0.3898	0.62
C_{12}	0.3039	-0.050
C_{13}	0.0694	0.1400
C_{16}	-0.008	0.0
C_{33}	0.1343	-0.300
C_{44}	0.0432	0.0910
C_{66}	0.0977	0.0610
Reference	[10]	[11]

TABLE I. Elements of elasticity tensors, in 10^{11} Pa. For tetragonal crystals, $C_{11} = C_{22}$, $C_{13} = C_{23}$, $C_{44} = C_{55}$, and $C_{16} = -C_{26}$.[12]

where D is in units analog-digital units (ADU), k_{pc} is in ADU-per-photon, and t_{dwell} is the dwell time. The conversion factor $k_{pc} = (1 - T_{pc}) \times QE \times Gain$, where T_{pc} is the transmission through the 3000-$\mathring{A}$–thick KBr photocathode. The net quantum efficiency QE of the photocathode accounts for production of secondary electrons by the KBr photocathode and their release into the streak tube[7] and monotonically increases from 11.3 to 12.4 photoelectrons per absorbed photon in the displayed spectral range of SXS. The average gain is 704 ADU per photoelectron and is the product of two factors: the mean of the streak camera pulse-height distribution (CCD electrons per photoelectron) and the CCD gain (ADU per CCD electron), both of which have been measured previously.[4] T_{filt} is the transmission of the 152.4-μm Be and 50.8-μm Al filters. The streak camera focuses the 200-μm width of the photocathode slit into a line-focus, while imaging the height of the slit at 0.4x magnification. Accounting for the 4x-binning applied to the data, the projected pixel area A_{eff} is then $(200\ \mu\text{m}) \times (13.5\ \mu\text{m}) \times 4/0.4 = 2.7 \times 10^{-}8\ \text{m}^2$. The dwell time varies monotonically from 4 to 6 ps/pixel throughout the experiment. Crystal reflectivities $R(E)$ were calculated using the PyTTE python package[8] with crystal structure from The Materials Project[9] and elasticity tensors as given in Table I.[10,11] Finally, the signal magnitude was cross-calibrated to the XRS spectrometer, multiplying the PJX signal by a factor of 0.74.

The spectral axis of SXS is calibrated *in situ* by modeling the spectral centroid of Cr $2p - 1s$ line emission.[13] This transition is photopumped by the core emission before the return shock ionizes the Cr, and thus originates from near-solid, weakly ionized Cr. The temperature at the beginning of the core flash is estimated to be 30 eV from the one-dimensional radiation-hydrodynamic code *LILAC*,[14] and a 10-eV uncertainty is assumed. At these temperatures, Cr is ionized into the M-shell, and the $2p - 1s$ lines from neighboring ionization states blend into a composite line that is blue-shifted relative to Cr K_α. The average ionization of the Cr is estimated from a screened-hydrogenic average-ion model[15,16] to be 6 ± 1.5 at these conditions. The shift of the composite line relative to K_α was calculated using FAC for an ensemble average over the set of lower states, giving a 2.8 ± 3.0 eV shift of the composite line relative to K_α. Analogous non-LTE calculations with PrismSPECT produce shifts of 6.3 ± 3.0 eV for the Stewart-Pyatt IPD model and 5.9 eV $\pm$ 2.5 eV for the Hummer-Mihalas IPD model, suggesting a +3.5 eV systematic uncertainty on the energy calibration and no change in the statistical uncertainty. The systematic uncertainty due to choice of atomic model is insufficient to change our conclusions.

The measured energy of this composite line will also be Doppler shifted by an amount that is less than the peak implosion velocity of 230 km/s. If the $2p-1s$ emission is optically thin, the front and rear hemispheres symmetrically broaden the Doppler profile with no shift. If the $2p-1s$ emission is optically thick, only emission from the front hemisphere is measured, and the line centroid shifts by $\frac{2}{3}\frac{v}{c}h\nu_0$. As a maximal estimate of uncertainty, we take the average of the two limiting cases to be the expectation value of the Doppler shift. Under these assumptions, the Doppler shift is -1.5 ± 0.5 eV.

The ionization shift and the Doppler shift together give a net shift of 1.3 ± 3.3 eV relative to K_α, where the uncertainties have been summed in quadrature. With this spectral calibrant, the remainder of the spectral axis is set using the dispersion calculated from the nominal dispersion of the spectrometer. The time-integrated XRS data reveals the same emission line plus seven absorption lines aligned between 5415 and 5640 eV (Fig. 5), giving confidence in the reality of these features and their relative photon energies.

The absorption features are robust to shot-to-shot variability. Fig. 5 shows the $1s-2p$ absorption band as measured by XRS across three separate experiments which changed only the core dopant. Shot 101967, which is presented in the main text, used 1% per atom of Kr dopant, while 101966 and 101968 used 1% per atom of Ar dopant. While the Ar dopant evidently photopumps the Cr fluorescence transition more than the Kr dopant, there is little change to the relative depth of the absorption features (indicative of ionization balance) and the relative position of the absorption features.

Radiative transfer model

The streaked spectrometer data is interpreted using a forward model of the spatially integrated emission escaping the target. The model conceives a blackbody core of radius R_c and temperature T_r concentric with and illuminating a hemispherical Cr shell of radius R and thickness Δ at temperature T and mass density ρ. The assumption of spherical symmetry is corroborated by time-gated x-ray pinhole images recorded simultaneously with the x-ray absorption spectra (Fig. 6).

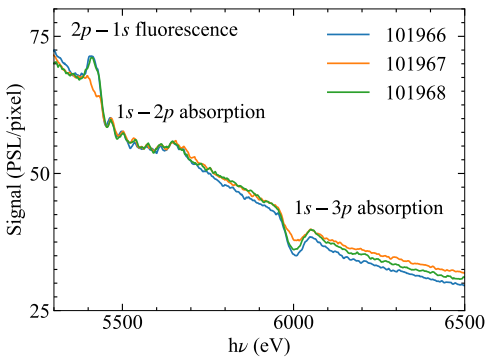


FIG. 5. Time-integrated spectra measured by XRS across three shots. Shot 101967 is described in the main text. Shots 101966 and 101968 used 1% per atom of Ar dopant instead of Kr, but were otherwise identical to Shot 101967. The lineouts are presented as raw signal (PSL) to highlight the repeatability of the absorption regions. A 3 PSL offset in the signal of 101967 was applied to account for shot-to-shot variation in the continuum emission.

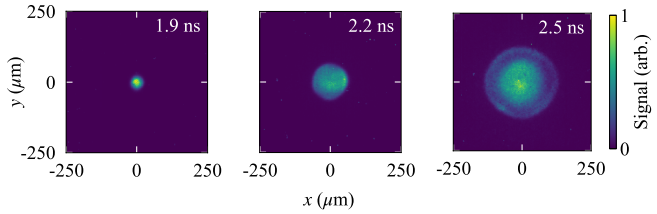


FIG. 6. X-ray pinhole images recorded before (1.9 ns), during (2.2 ns), and after (2.5 ns) the x-ray absorption data was collected.

Due to the high densities achieved at stagnation, the Cr is assumed to be in local thermodynamic equilibrium,[15] such that its source function is a Planckian spectrum B_ν at temperature T. The validity of local thermodynamic equilibrium (LTE) is further verified by comparing LTE and non-LTE calculations of *PrismSPECT*.[17] Parallel rays are propagated through this geometry by solving the equation of radiative transfer. The emerging spectral radiance is then integrated over area to obtain the source emission rate $\dot{S}_\nu \equiv \frac{\mathrm{d}S_\nu}{\mathrm{d}t}$, the same quantity recorded by the time-resolved, spatially integrating spectrometer. Assuming a thin shell ($\Delta << R$) the following analytic solution is obtained:

$$\dot{S}_\nu = \pi R^2 B_\nu(T_r)\left[(1-\tau_\nu)e^{-\tau_\nu} - (1-b)\left(1-\frac{\tau_\nu}{\sqrt{1-b}}\right)\exp\left(\frac{-\tau_\nu}{\sqrt{1-b}}\right) + \tau_\nu^2\left[\mathrm{Ei}\left(\frac{-\tau_\nu}{\sqrt{1-b}}\right) - \mathrm{Ei}(-\tau_\nu)\right]\right]$$
$$+ \pi R^2 B_\nu(T)\left[1-(1-\tau_\nu)e^{-\tau_\nu} + \tau_\nu^2\mathrm{Ei}(-\tau_\nu) + (a-1) - \frac{2}{(\alpha_\nu R)^2}\left(1-(1+\alpha_\nu R\sqrt{a-1}\,)\exp\left(-\alpha_\nu R\sqrt{a-1}\,\right)\right)\right], \quad (3)$$

where $a = (1+\Delta/R)^2$, $b = (R_c/R)^2$, $\tau_\nu = \kappa_\nu \rho \Delta$, and $\mathrm{Ei}(x) = -\int_{-x}^{\infty} \mathrm{d}t\; t^{-1}e^{-t}$ is the exponential integral. The solution is the sum of core emission transmitted by the shell and self-emission from the shell, thus encoding the geometry, thermodynamic state, and radiative properties of the core and Cr shell. Rapid calculation of the exponential integral necessary for the many thousands of Monte Carlo samples was enabled by the approximation found in Ref.[18].

The spectral opacity κ_ν of the Cr shell is modeled as the sum of seven Gaussian lineshapes, one for each composite line denoted by the index i. Each composite line uses a parametrized frequency-integrated opacity $\kappa^{(i)} = \int d\nu\, \kappa_\nu^{(i)}(T,\rho)$ that encodes the ionization balance. Anticipating shifted and broadened lines, line centroids $h\nu_i$ and line widths σ_i are free parameters to be inferred from the measurements.

Opacity model

The multicomplex screened hydrogenic model calculates the opacity contribution of different states with prescribed shell populations. The screened hydrogenic formalism[19–21] is used to determine the energy of each included state. Excited states of L-shell ions with a maximum principal quantum number $n_{max} = 3$ are included, as well as He- and Ne-like states. L-shell complexes

with higher shells occupied and all M-shell complexes are predicted to be pressure ionized at the relevant conditions, justifying their exclusion from the model. At the high densities of the compressed Cr, LTE is expected to hold,[15] and the population density N_i of each complex i adheres to Saha-Boltzmann statistics modified by an Ecker-Kröll ionization-potential-depression (IPD) model.[22] *PrismSPECT*[17] calculations indicate negligible difference between the ionization balance, opacity magnitude, and line centroids of LTE versus non-LTE at the relevant conditions. The average ionization $\bar{Z}$ is calculated in a screened-hydrogenic average-ion model[15,16] and used as input for the IPD model.

The opacity model uses population densities defined for initial (final) complexes i (j) and oscillator strengths defined for angular-momentum–resolved configurations μ (η). The multielectron configuration oscillator strengths are defined in terms of the hydrogenic oscillator strengths $f^H_{\eta\mu}$ summed over j and m_j of final states and averaged over j and m_j of initial states:[23]

$$f_{\eta\mu} = w_\mu \frac{4\ell_\eta + 2 - w_\eta}{4\ell_\eta + 2}\, f^H_{\eta\mu}, \tag{4}$$

where w_μ is the initial occupation of the source orbital ($1s$) and the second term is the probability that the destination orbital with angular momentum ℓ_η and occupation w_η is initially occupied. For $1s-2p$ absorption, $f^H_{\eta\mu} = 0.4162$. The opacity for bound-bound transitions is then

$$\kappa_\nu = \frac{\pi r_0 c}{A m_p N} \sum_i \left[\mathcal{L}_{ji}(\nu) \frac{N_i}{g_i} \sum_{\mu\in i} g_\mu f_{\eta\mu} \right] \tag{5}$$

$$g_\mu = \prod_{n=1}^{n_{max}} \prod_{\ell=0}^{n-1} \binom{2\ell+2}{w_{n\ell}} \tag{6}$$

$$g_i = \prod_{n=1}^{n_{max}} \binom{2n^2}{P_n} \tag{7}$$

where $\mathcal{L}_{ji}(\nu)$ is the normalized line-shape function, $N = \sum_i N_i$ is the total ion density, P_n is the occupation of shell n, and g_μ and g_i are the statistical weights of initial configurations and initial complexes, respectively. For this analysis, a Gaussian lineshape of each composite line i has been assumed.

Inference

The forward model is applied within a Bayesian inference framework to simultaneously constrain the posterior probability distributions of the twenty model parameters. A No U-Turn Sampler (NUTS)[24,25] is used to efficiently sample the posterior space using 5000 samples in each of four chains. Each prior is a Gaussian distribution, with physically imposed lower or upper limits. The conditional limits $R > R_c$ and $T < T_r$ are also imposed (see Table II). The resulting fit to the lineout at 2.24 ns is shown in Fig. 7, where a higher-energy range around 5900 eV is included in the fit to constrain the continuum components.

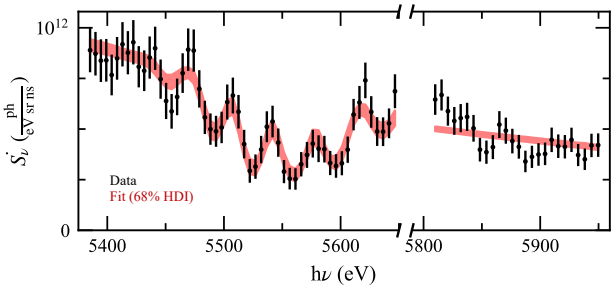


FIG. 7. Measured source emission rate $\dot{S}_\nu$ (black) averaged between 2.20 and 2.28 ns of the streak record. The red band shows the 68% highest density interval (HDI) of the inference. Data between 5650 and 5800 eV is obscured by a camera defect and is omitted.

Variable	Distribution	μ	σ	Lower	Upper	Units
R	TruncatedNormal	80.0	50	0		μm
R_c	TruncatedNormal	50.0	25	0		μm
ρ	TruncatedNormal	40	20	1.0	100.0	g/cm^3
T_r	Normal	600	100			eV
T	Normal	400	50	50.0	1000.0	eV
$\log_{10}(\ell)$	Normal	0	1			$\log_{10}(\mu\text{m})$
$h\nu_0$	Normal	5420	10			eV
$h\nu_1$	Normal	5450	10			eV
$h\nu_2$	Normal	5485	10			eV
$h\nu_3$	Normal	5522	10			eV
$h\nu_4$	Normal	5556	10			eV
$h\nu_5$	Normal	5598	10			eV
$h\nu_6$	Normal	5630	10			eV
σ_0	TruncatedNormal	10	2	2		eV
σ_1	TruncatedNormal	10	2	2		eV
σ_2	TruncatedNormal	10	2	2		eV
σ_3	TruncatedNormal	10	2	2		eV
σ_4	TruncatedNormal	10	2	2		eV
σ_5	TruncatedNormal	10	2	2		eV
σ_6	TruncatedNormal	10	2	2		eV

TABLE II. Gaussian prior distributions with mean μ, standard deviation σ, and lower and upper limits (where present). All lengths are in μm; temperatures, photon energies, and line widths are in eV; and density is in g/cm^3.

The ionization, inferred from the presence of different absorption features, is observed to increase in time (Fig. 8). Though conditional on the chosen atomic model, the temperature and density inferred from the Cr ionization balance indicate significant heating of the Cr during stagnation (Fig. 9 (a)). The inferred density, with notably broader highest-density intervals (HDI) inherited from the weak dependence of the opacity and ionization balance on ρ, suggest that the Cr shell is temporarily confined by the outer-lying plastic. This behavior is caused by the outer shell impacting the Cr layer

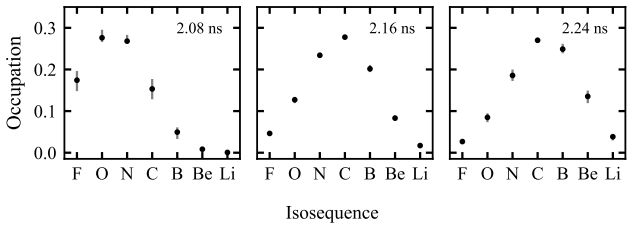


FIG. 8. Ionization balance inferred from each absorption spectrum, denoted by the central time of the measurement. Error bars denote the 68% HDI.

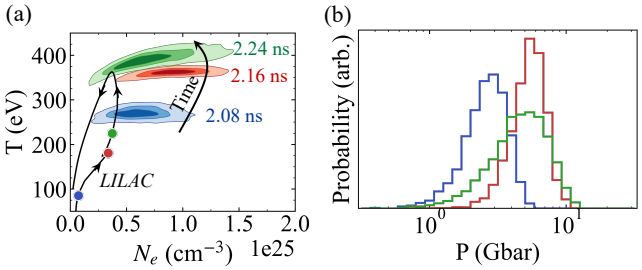


FIG. 9. (a) Posterior probability distributions of T and N_e from fits to the Cr absorption spectra assuming the Ecker-Kröll IPD model. The 30%, 60%, and 90% HDIs are shown at 2.08 ns (blue), 2.16 ns (red), and 2.24 ns (green). LILAC-simulated conditions of the Cr layer are shown by the black line, and simulated conditions co-timed with the measurements are indicated by the colored points. (b) Posterior probability distributions of pressure assuming the SESAME equation of state 3070.

before the return shock breaks out and the shell disassembles. One-dimentional radiation-hydrodynamic simulations with the *LILAC*[14] code, adjusting the input laser energy and heat transport model of the ablation to match the observed x-ray bang-time (i.e. time of peak x-ray emission at photon energies between 5 and 6 keV), provide a comparative picture for this complex implosion (Fig. 2). Temperatures inferred from our data are comparable to peak simulation temperatures, while inferred densities are larger than and occur earlier in time than peak densities in simulations (Fig. 9).

Corresponding posterior distributions of the pressure from the SESAME equation of state 3070[26] are shown in Fig. 9 (b). The ranges of the distributions mostly lie between 1 and 10 Gbar (100 and 1000 TPa) with uncertainties in $\log_{10}(P/(1\text{ Gbar}))$-space ranging from less than 0.1 at 2.16 ns to 0.5 at 2.08 ns. This should be compared to the time-resolved self-emission image analysis of Ruby *et al.*[27] which inferred a peak hot-spot pressure from synthetic implosions as $\log_{10}(P/(1\text{ Gbar})) = 1.08 \pm 0.18$. Though there is value in extending such a mechanical model to provide an independent measurement of the shell pressure, doing so does not seem to substantially reduce the uncertainties in pressure.

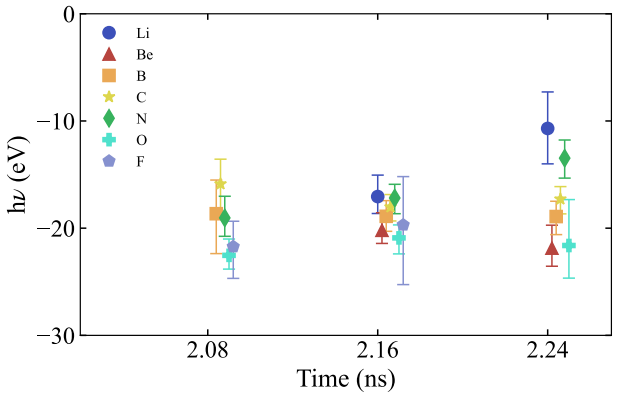


FIG. 10. All measured residual line shifts labeled by isoelectronic sequence, calculated as the observed line energy minus the isolated atom theoretical line energy, the inferred Doppler shift, and the inferred contribution from excited states. Error bars denote the quadrature sum of the 68% HDI of each shift component.

The residual line shift that is not accounted for by the Doppler shift or excited states is significantly different from zero for all measured ionization states at each time (Fig. 10). While there does appear to be a systematic Z-dependence to the shift, our uncertainty makes it difficult to provide a strong statement on this dependence. The posterior distribution of the Doppler shift is calculated as $\Delta h\nu_{\text{Doppler}} = \frac{v}{c} h\nu_0$, where v is the velocity of the Cr shell calculated from the inferred Cr radius, c is the speed of light, and $h\nu_0$ is the transition energy without Doppler shift. The posterior distributions of the satellite shifts are calculated from the screened hydrogenic model as

$$\Delta h\nu_{\text{satellite}} = h\nu(T=0) - \int \mathrm{d}T\ f(T)\ h\nu(T), \qquad (8)$$

where $h\nu(T=0)$ is the transition energy involving only the ground state (i.e. at temperature $T = 0$), $f(T)$ is the posterior distribution of T, and $h\nu(T)$ is the temperature-dependent line centroid. Both $h\nu(T=0)$ and $h\nu(T)$ are calculated with the screened hydrogenic model.

For comparison, the spectra were also fit assuming a Stewart-Pyatt IPD model. As seen in Fig. 11, the inferred temperature is roughly constant in time while the density catastrophically decompresses, which runs contrary to the expected behavior of the dense-plastic–tamped Cr shell at stagnation.

Line shift models

The Debye (D) and uniform electron gas (UEG) models shown in Fig. 4 are derived assuming a first-order perturbation of hydrogenic wavefuctions. The perturb-

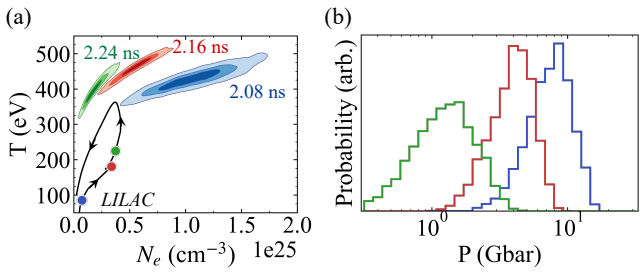


FIG. 11. Same as Fig. 9 but a Stewart-Pyatt IPD model was assumed, inferring rapid decompression.

ing potentials V,[28,29] energy level shifts ΔE,[30] and transition energy shifts $\Delta h\nu$[29] are:

$$V_{\mathrm{D}} = \frac{1}{4\pi\epsilon_0}\frac{Ze^2}{r}\left[\frac{r}{\lambda_D} - \frac{1}{2}\left(\frac{r}{\lambda_D}\right)^2\right] \tag{9}$$

$$\Delta E_{\mathrm{D}} = \frac{1}{4\pi\epsilon_0}\frac{Ze^2}{\lambda_D}\left(1 - \frac{\langle r\rangle_{n\ell}}{2\lambda_D}\right) \tag{10}$$

$$\Delta h\nu_{\mathrm{D}} = -\frac{1}{4\pi\epsilon_0}\frac{Ze^2}{\lambda_D}\left(\frac{\langle r\rangle_2 - \langle r\rangle_1}{2\lambda_D}\right) \tag{11}$$

$$V_{\mathrm{UEG}} = \frac{3}{8\pi\epsilon_0}\frac{Ze^2}{R_0}\left(1 - \frac{1}{3}\frac{r^2}{R_0^2}\right) \tag{12}$$

$$\Delta E_{\mathrm{UEG}} = \frac{3}{8\pi\epsilon_0}\frac{Ze^2}{R_0}\left(1 - \frac{1}{3}\frac{\langle r^2\rangle_{n\ell}}{R_0^2}\right) \tag{13}$$

$$\Delta h\nu_{\mathrm{UEG}} = -\frac{1}{4\pi\epsilon_0}\cdot\frac{2}{3}\pi N_e e^2\left(\langle r^2\rangle_2 - \langle r^2\rangle_1\right) \tag{14}$$

$$\tag{15}$$

with ion charge Z, radial moments $\langle r^i\rangle_{n\ell} \equiv \int_0^\infty r^i |P_{n\ell}(r)|^2\,\mathrm{d}r$ of hydrogenic orbitals $n\ell$, Debye length $\lambda_D = \left(\frac{\epsilon_0}{e^2}\frac{kT}{N_e}\right)^{1/2}$, and ion sphere radius $R_0 = \left(\frac{4\pi}{3}N_i\right)^{-1/3}$. The screened nuclear charge Q_n calculated from a screened-hydrogenic average-atom model is used in place of the nuclear charge Z to better model non-hydrogenic atoms within this hydrogenic picture.

The DFT-based opacity of Fig. 3 (a) is based on a previously published method,[31,32] in which a density-functional-theory–molecular-dynamics (DFT-MD) simulation of Cr atoms is performed and the Kohn-Sham orbitals from each time step are retained. A vacancy in the $1s$ orbital of each atom simulates photoionization and enables a Kubo-Greenwood calculation[33,34] of the photon energy and relative oscillator strength of the $2p-1s$ emission. The opacity is derived by assuming detailed balance.

* bishel1@llnl.gov

[1] Thorn, D. B. *et al.* X-ray spectrometer throughput model for (selected) flat Bragg crystal spectrometers on laser plasma facilities. *Review of Scientific Instruments* **89** (2018).

[2] Millecchia, M., Regan, S. P., Bahr, R. E., Romanofsky, M. & Sorce, C. Streaked x-ray spectrometer having a discrete selection of Bragg geometries for Omega. *Review of Scientific Instruments* **83**, 1–4 (2012).

[3] Gotchev, O. V., Jaanimagi, P. A., Knauer, J. P., Marshall, F. J. & Meyerhofer, D. D. KB-PJX-A streaked imager based on a versatile x-ray microscope coupled to a high-current streak tube (invited). *Review of Scientific Instruments* **75**, 4063–4068 (2004).

[4] Ivancic, S. T. An Ultrafast X-Ray Streak Camera for Time-Resolved High-Energy-Density Applications. *LLE Review* **153**, 17–23.

[5] Marrs, R. E., Brown, G. V., Emig, J. A. & Heeter, R. F. System for calibrating the energy-dependent response of an elliptical Bragg-crystal spectrometer. *Review of Scientific Instruments* **85**, 11D626 (2014).

[6] Maddox, B. R. *et al.* High-energy x-ray backlighter spectrum measurements using calibrated image plates. *Review of Scientific Instruments* **82** (2011).

[7] Henke, B. L., Knauer, J. P. & Premaratne, K. The characterization of x-ray photocathodes in the 0.1-10-keV photon energy region. *Journal of Applied Physics* **52**, 1509–1520 (1981).

[8] Honkanen, A. P. & Huotari, S. General method to calculate the elastic deformation and X-ray diffraction properties of bent crystal wafers. arXiv (2020). https://doi.org/10.48550/arXiv.2006.04952.

[9] Jain, A. *et al.* Commentary: The materials project: A materials genome approach to accelerating materials innovation. *APL Materials* **1** (2013).

[10] Haussuhl, S. Elastic and thermoelastic properties of selected organic crystals: acenaphthene, trans-azobenzene, benzophenone, tolane, trans-stilbene, dibenzyl, diphenyl sulfone, 2,2´-biphenol, urea, melamine, hexogen, succinimide, pentaerythritol, urotropine, malonic. *Zeitschrift für Kristallographie* **216**, 339–353 (2001).

[11] Haynes, W. M. (ed.) *CRC Handbook of Chemistry and Physics* (CRC Press, 2012).

[12] Duffy, T. & Delamater-Droungas, R. Single-Crystal Elasticity Database. .

[13] Saemann, A. *et al.* Isochoric heating of solid aluminum by ultrashort laser pulses focused on a tamped target. *Physical Review Letters* **82**, 4843–4846 (1999).

[14] Delettrez, J., Epstein, R., Richardson, M. C., Jaanimagi, P. A. & Henke, B. L. Effect of laser illumination nonuniformity on the analysis of time-resolved x-ray measurements in uv spherical transport experiments. *Physical Review A* **36**, 3926–3934 (1987).

[15] Bishel, D. T. *et al.* Toward constraint of ionization-potential depression models in a convergent geometry. *High Energy Density Physics* **50** (2024).

[16] Bishel, D. T. AtPhys: Atomic Physics Package (2023). `https://doi.org/10.5281/zenodo.10045187`.

[17] MacFarlane, J. J. *et al.* Simulation of the ionization dynamics of aluminum irradiated by intense short-pulse lasers. In Hammel, B. A., Meyerhofer, D. D., Meyer-ter Vehn, J. & Azechi, H. (eds.) *Inertial Fusion Sciences and Applications 2003*, 457–460 (American Nuclear Society, La Grange Park, IL, 2003).

[18] Barry, D. A., Parlange, J. Y. & Li, L. Approximation for the exponential integral (Theis well function). *Journal of*

Hydrology **227**, 287–291 (2000).

[19] Mayer, H. Methods of opacity calculations, Atomic Energy Commission Reports, Los Alamos Scientific Laboratory. 1–151 (Los Alamos, NM, 1947). Https://permalink.lanl.gov/object/tr?what=info:lanl-repo/lareport/LA-00647.

[20] Epstein, R. Satellite absorption lines and the temperature dependence of x-ray absorption features in high-temperature plasmas. *Physical Review A* **43**, 961–967 (1991).

[21] Atzeni, S. & Meyer-ter Vehn, J. *The Physics of Inertial Fusion : Beam Plasma Interaction, Hydrodynamics, Hot Dense Matter* (Oxford University Press, Oxford, United Kingdom, 2004).

[22] Ecker, G. & Kröll, W. Lowering of the ionization energy for a plasma in thermodynamic equilibrium. *Physics of Fluids* **6**, 62–69 (1963).

[23] Griem, H. R. *Principles of Plasma Spectroscopy* (Cambridge University Press, New York, 2005).

[24] Bingham, E. *et al.* Pyro: Deep universal probabilistic programming. *Journal of Machine Learning Research* **20**, 1–6 (2019).

[25] Phan, D., Pradhan, N. & Jankowiak, M. Composable Effects for Flexible and Accelerated Probabilistic Programming in NumPyro. arXiv (2019). https://doi.org/10.48550/arXiv.1912.11554.

[26] Lyon, S. P. & Johnson, J. D. *SESAME: The Los Alamos National Laboratory Equation of State Database, Report LA-UR-92-3407* (Los Alamos, NM, 1992).

[27] Ruby, J. J., Gaffney, J. A., Rygg, J. R., Ping, Y. & Collins, G. W. High-energy-density-physics measurements in implosions using Bayesian inference. *Physics of Plasmas* **28**, 032703 (2021).

[28] Sakurai, J. & Napolitano, J. *Modern Quantum Mechanics* (Cambridge University Press, New York, 2017).

[29] Skupsky, S. X-ray line shift as a high-density diagnostic for laser-imploded plasmas. *Physical Review A* **21**, 1316–1326 (1980).

[30] More, R. M. Electronic Energy Levels in Dense Plasmas. *J. Quant. Spectrosc. Radiat. Transfer* **27**, 345–357 (1982).

[31] Hu, S. X. *et al.* Probing atomic physics at ultrahigh pressure using laser-driven implosions. *Nature Communications* **13**, 6780 (2022).

[32] Hu, S. X. *et al.* VERITAS: A density-functional theory-based multiband kinetic model for understanding x-ray spectroscopy of dense plasmas. *Physics of Plasmas* **32**, 073303 (2025).

[33] Kubo, R. Statistical-Mechanical Theory of Irreversible Processes. I. General Theory and Simple Applications to Magnetic and Conduction Problems. *Journal of the Physical Society of Japan* **12**, 570–586 (1957).

[34] Greenwood, D. A. The Boltzmann Equation in the Theory of Electrical Conduction in Metals. *Proceedings of the Physical Society* **71**, 585 (1958).

Acknowledgments: This material is based upon work supported by the Department of Energy [National Nuclear Security Administration] University of Rochester "National Inertial Confinement Fusion Program" under Award Number(s) DE-NA0004144, and the NSF Physics Frontier Center, Center for Matter at Atomic Pressures (CMAP), under Award PHY-2020249. This work performed under the auspices of the U.S. Department of Energy and an appointment to the Office of Science, by Lawrence Livermore National Laboratory under Contract DE-AC52-07NA27344.

This report was prepared as an account of work sponsored by an agency of the United States Government. Neither the United States Government nor any agency thereof, nor any of their employees, makes any warranty, express or implied, or assumes any legal liability or responsibility for the accuracy, completeness, or usefulness of any information, apparatus, product, or process disclosed, or represents that its use would not infringe privately owned rights. Reference herein to any specific commercial product, process, or service by trade name, trademark, manufacturer, or otherwise does not necessarily constitute or imply its endorsement, recommendation, or favoring by the United States Government or any agency thereof. The views and opinions of authors expressed herein do not necessarily state or reflect those of the United States Government or any agency thereof. LLNL-JRNL-872994.

Data Availability: Data recorded for the experiment will be openly available at https://dx.doi.org/10.60593/ur.d.28931213 once the data embargo has been lifted (07-05-2026). Before the end of the data embargo, all relevant data are available from the authors upon reasonable request.

Author Contributions: D.T.B., P.M.N., G.W.C. and J.R.R conceptualized and proposed the experiment. The experiment was executed by D.T.B., D.A.C., J.J.R., and P.M.N. The data analysis methodology was developed by D.T.B. with D.A.C., E.A.S., J.J.R., and M.A.S codeveloping statistical tools and providing feedback. P.M.N., E.V.M., S.H., G.W.C. and R.E. assisted with data interpretation and construction of the spectral model. S.H. provided both hydrodynamic simulations and the DFT-based atomic kinetics results. M.F.G. and I.G. assisted with FAC models of density-dependent line shifts. D.T.B. wrote the manuscript with help from P.M.N., D.A.C., E.A.S., S.H., J.R.R., and G.W.C.

* bishel1@llnl.gov